EES Batteries

ROYAL SOCIETY OF CHEMISTRY

PAPER

View Article Online
View Journal

Cite this: DOI: 10.1039/d6eb00031b

Tailored the polymer interface of Prussian blue analogues for sodium-ion batteries

Parham Pirayesh,[a] Enzhong Jin,[a] Yijia Wang,[a] Zhi Liang Dong,[a] Yi Gan,[a] Yi Yuan,[a] Mingrui Yang,[a] Reza Andaveh,[a] Frederick Benjamin Holness,[a] Shin-An Chen,[c] Lo-Yueh Chang,[c] Xin Pang[b] and Yang Zhao *[a]

The development of long-life sodium-ion batteries (SIBs) hinges on stable cathode–electrolyte interfaces. Fe-based Prussian blue analogues (PBAs) are promising cathodes for SIBs, valued for their low cost and open framework that facilitates rapid three-dimensional Na^+ diffusion. However, their practical application is severely limited by poor long-term cycling stability, a challenge primarily attributed to the formation of a fragile and chemically unstable cathode–electrolyte interphase (CEI). This natural CEI promotes parasitic side reactions that consume active Na^+ inventory, increase interfacial impedance, and accelerate capacity fade. Here, we introduce a strategy to overcome this limitation by engineering a conformal, and nanoscale artificial CEI using a functionalized linked polymer (FLP). This engineered interphase acts as a robust physical and chemical barrier, effectively suppressing parasitic electrolyte decomposition, mitigating active material dissolution, and preserving the structural integrity of the cathode by buffering against chemo-mechanical strain. These findings establish key design principles for artificial CEIs, emphasizing conformality, mechanical compliance, and controlled thickness, providing a scalable route to high-performance, long-life Na-ion cathodes.

Received 6th February 2026,
Accepted 25th March 2026

DOI: 10.1039/d6eb00031b

rsc.li/EESBatteries

Broader context

Sodium-ion batteries (SIBs) are emerging as a compelling alternative to lithium-ion batteries for large-scale energy storage due to the abundance, low cost, and wide geographic distribution of sodium. However, the long-term durability of SIB cathodes remains a major barrier to their widespread adoption, particularly for grid-level applications where extended cycle life and reliability are essential. Interfacial instability between cathode materials and electrolytes leads to parasitic reactions, impedance growth, and rapid capacity degradation, undermining performance and safety. Fe-based Prussian blue analogues offer an attractive cathode platform because of their open framework and fast sodium-ion transport, yet their practical viability is constrained by unstable cathode–electrolyte interphases. This work addresses a fundamental interfacial challenge by demonstrating a scalable artificial CEI design that enhances chemical stability, mechanical resilience, and interfacial integrity. Beyond Prussian blue analogues, the design principles established here with conformal coverage, nanoscale thickness control, and mechanical compliance are broadly applicable to other sodium-ion and multivalent battery chemistries. These insights advance the rational engineering of stable electrochemical interfaces, contributing to the development of durable, cost-effective energy storage technologies for a sustainable energy future.

Introduction

The growing demand for large-scale, cost-effective energy storage has accelerated interest in the sodium-ion batteries (SIBs) as a complementary technology to lithium-ion systems, driven by the natural abundance and low cost of Na.[1–3] In practical SIBs, the cathode plays a decisive role by supplying the reversible Na^+ inventory in full cells. Among various cathodes for SIBs, such as layered transition-metal oxides, polyanionic compounds, and Prussian blue analogues (PBAs),[4,5] Fe-based PBAs have emerged as particularly attractive candidates due to their fast three-dimensional Na^+ transport, low-strain host lattice, and competitive theoretical capacities, which together promise long cycle life and low cost.[6–8]

Despite these structural merits, Fe-based PBA cathodes still suffer from capacity fading and impedance growth, now widely attributed to the instability of the natural cathode–electrolyte interphase (CEI) formed at high potentials.[9,10] At elevated states of charge, highly oxidized Fe centers catalyze electrolyte oxidation, producing natural CEIs enriched with alkyl carbonates, Na_2CO_3, and NaF.[11–13] When this interphase is mechanically fragile or chemically unstable, it undergoes repeated

---

[a] Department of Mechanical and Materials Engineering, University of Western Ontario, London, Ontario, N6A 5B9, Canada. E-mail: yzhao628@uwo.ca
[b] CanmetMATERIALS, Natural Resources Ca, nada183 Longwood Road South, Hamilton, ON L8P 0A5, Canada
[c] National Synchrotron Radiation Research Center, Hsinchu 300092, Taiwan

rupture and re-formation that (i) consumes the active Na^+ inventory, (ii) thickens the CEI, hindering ion transport, and (iii) increases charge-transfer resistance, collectively accelerating performance degradation.[14–17]

In addition, the interfacial instability is further amplified by intrinsic bulk defects and crystal water. Conventional co-precipitation routes often introduce $[Fe(CN)_6]$ vacancies and water molecules that occupy Na^+ sites, distort local fields, and catalyze unwanted chemical reactions at the interface. Recent studies confirm that, $[Fe(CN)_6]$ vacancies and residual water (zeolitic, interstitial/structural, or ligand-coordinated) deteriorate cycling by distorting the framework, hindering Na^+/electron transport, increasing polarization, and triggering high-voltage side reactions *via* $Na(OH_2)^+$ extraction; accordingly, vacancy-lean, low-water PBAs exhibit superior cycling stability to vacancy-rich, hydrated analogues.[18–21] On the other hand, electrolyte formulation further tunes CEI evolution on PBAs. Direct comparisons between NaTFSI- and $NaClO_4$-based electrolytes show that their distinct solvation and hydration behaviors alter the reactivity of crystal water, shift Fe oxidation pathways, and ultimately dictate CEI composition.[22,23] These findings underscore the need to interpret CEI chemistry in the context of both lattice structure and electrolyte environment. Yet, even with optimized electrolytes and improved synthesis routes, the natural CEI remains chemically heterogeneous and mechanically fragile under extended cycling.

Taken together, these insights motivate a strategic shift; rather than tolerating a continuously evolving natural CEI, a deliberately engineered artificial CEI can be imposed on Prussian blue (PB) particles to passivate reactive sites while maintaining Na^+ transport. Recent studies converge on design principles for effective artificial CEIs, independent of coating chemistry, including (i) conformal and continuous coverage to prevent ongoing electrolyte decomposition and interfacial side reactions, (ii) nanometric thickness to balance passivation with ionic flux, and (iii) mixed transport properties tuned to suppress parasitic reactions without throttling charge transfer.[10,13,24,25] Zhang *et al.* demonstrated that an inorganic oxide passivation film, specifically, a conformal ZnO layer, on Prussian white preserves the monoclinic structure and markedly improves air and cycling stability under humid conditions, underscoring the broad utility of protective artificial interphases.[26] Compared with inorganic coatings, organic polymer interphases offer advantages beyond improved surface conductivity when used as artificial CEIs. Their mechanical compliance buffers (de)sodiation-induced strain, accommodating volume change and limiting particle cracking/delamination, while their electronic/chemical functionality can improve electrolyte wettability and enable intimate cathode–electrolyte contact. Conductive polymers such as polyaniline (PANI)[27,28] and polypyrrole (PPy)[29,30] have been used to passivate the PB interface, enhancing rate capability and cycling stability. Recently, functional linked polymers (FLP) have attracted growing attention as artificial interphases and protective coatings for electrodes. The FLP combines high elasticity, strength, and chemical stability, yielding compliant films that buffer (de)sodiation-induced strain and preserve interfacial integrity. Its nitrogen-bearing polar groups help regulate Na-ion fluxes, promoting uniform Na deposition.[31–34]

Beyond PBAs, interfacial instability and chemo-mechanical damage are universal failure modes in SIBs. In layered transition-metal oxide cathodes, repeated (de)sodiation can trigger anisotropic lattice strain, phase transitions, microcracking, and surface reconstruction, which collectively destabilize the CEI and accelerate impedance rise and capacity fade; accordingly, recent work emphasizes synergistic interface engineering and structural modulation as key stabilization routes for layered oxides.[35] In parallel, for conversion and alloying anodes, large volume expansion and repeated interphase rupture/reformation lead to loss of electrical contact and continuous SEI growth; thus, strategies that couple interface regulation with mechanical buffering frameworks (*e.g.*, conductive confinement, elastic matrices, and stress-accommodating architectures) are increasingly adopted to sustain cycling stability.[36,37]

Motivated by these cross-cutting principles, we apply an interphase design to PBAs by constructing a conformal, mechanically compliant nanoscale FLP as the artificial CEI for long-term stable Fe-based PB cathodes. By precisely controlling the nanometric thickness of the coating, the optimized FLP layer (~8 nm) delivers a mechanically compliant yet chemically robust interphase that effectively suppresses electrolyte decomposition, mitigates active material dissolution, and buffers particle strain during repeated cycling. As a result, the FLP-coated PB cathodes achieve more stable performances over 3000 cycles at 5C, far surpassing uncoated counterparts. Structurally, the FLP layer suppresses lattice breathing, as *ex situ* XRD after extended cycling shows sharp reflections with only small, reversible shifts, whereas pristine PB exhibits broadened, displaced peaks. Spectroscopically, the $\nu(C{\equiv}N)$ Raman response of 25@FLP-PB remains nearly position-invariant through (de)sodiation, indicating mitigated strain. Interfacially, X-ray photoelectron spectroscopy (XPS) after long-term cycling preserves the urea-linkage N feature near 400 eV and shows a CEI enriched in NaF and fluorinated organics, demonstrating a chemically robust, mechanically compliant inorganic–organic interphase that passivates parasitic reactions and underpins the superior capacity retention. This work provides fundamental insights into how artificial interphases regulate electrochemical and structural stability, while offering a scalable, broadly applicable strategy to realize durable SIBs through interphase-focused design.

Results and discussion

Polyurea as an FLP was selected to construct an artificial CEI layer for PB because its dense hydrogen-bond network and polar functionalities promote strong adhesion with the substrate surface and facilitate Na^+ transport.[31,32,38] A molecule-level, uniform, thickness-controlled FLP layer was deposited on PB by molecular layer deposition (MLD), as schematized in

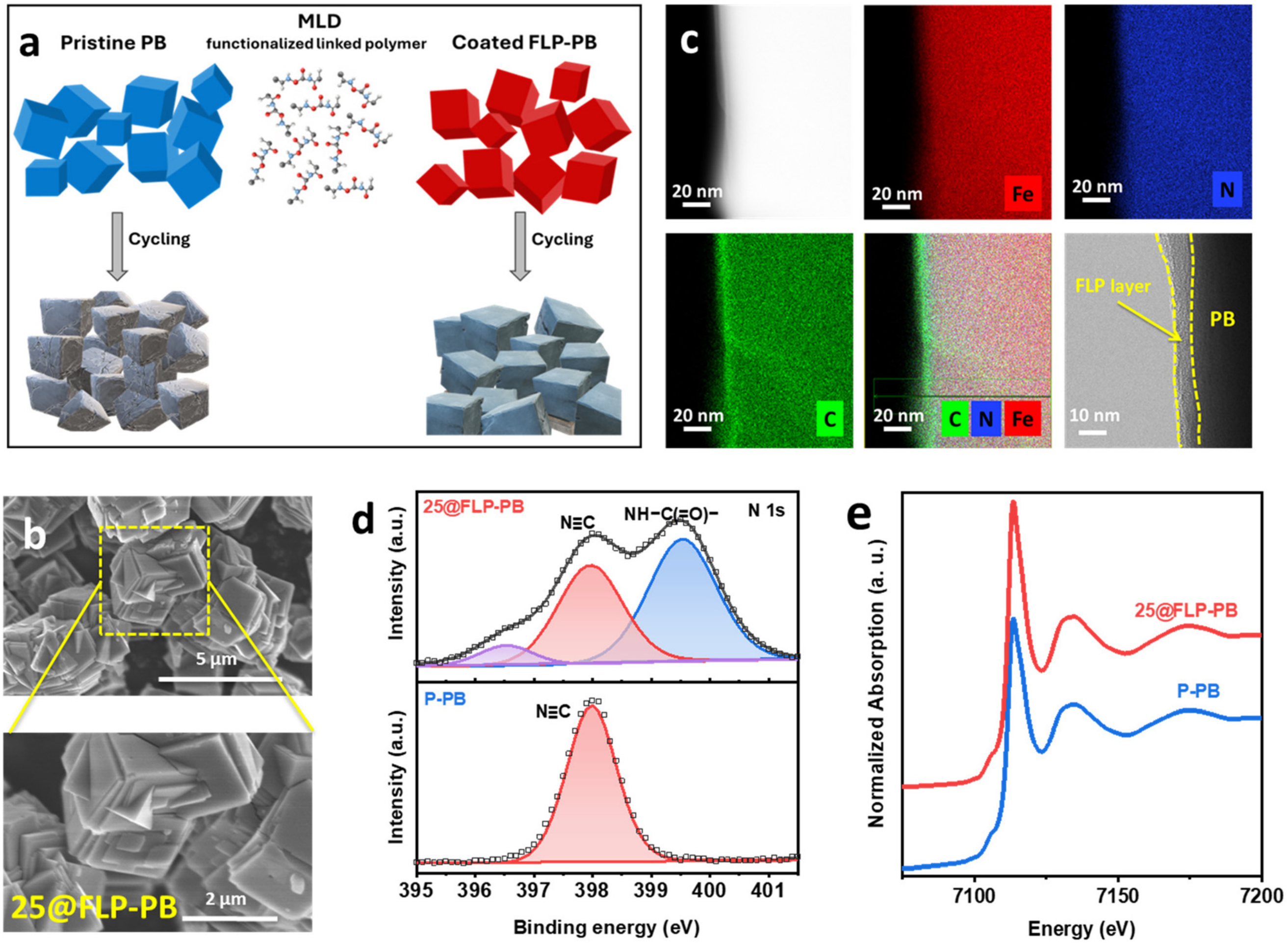

Fig. 1 (a) Schematic of the MLD process for coating PB cathodes with an FLP film. (b) SEM image of 25@FLP-PB particles. (c) High-resolution TEM image of a 25@FLP-PB particle. (d) N 1s XPS spectrum of the 25@FLP-PB sample. (e) Fe K-edge XANES spectra for pristine and coated PB samples.

Fig. 1a. Growth proceeds *via* alternating, self-limiting exposures of 1,4-phenylene diisocyanate (PDIC) and ethylenediamine (ED): surface –OH/H_2O sites on PB first react with PDIC to generate an isocyanate-terminated surface (Step 1), which then couples with ED to form urea linkages (Step 2). Repeating this PDIC/ED sequence constitutes one binary cycle; iterating cycles yields a conformal coating with nano-level thickness control.[38] To systematically investigate the influence of the coating on the properties of the cathode, FLP layers of varying thicknesses were applied by controlling the number of MLD cycles. The resulting samples, coated with 10, 25, and 50 cycles, were denoted as 10@FLP-PB, 25@FLP-PB, and 50@FLP-PB, respectively.

The morphology of the pristine and coated hexacyanoferrate particles was first examined using scanning electron microscopy (SEM). The pristine PB (P-PB) particles exhibit a cubic morphology with dimensions ranging from approximately 2–3 μm (Fig. S1, SI). As shown in Fig. 1b, the overall particle morphology and size remained unchanged after the application of the FLP coating, confirming that the MLD process does not alter the bulk structure of the cathode material. To maintain consistency in our detailed analysis, the 25@FLP-PB sample was selected as a representative condition for further characterization. To confirm that the underlying crystal structure of the host material was preserved, X-ray diffraction (XRD) was also performed. The XRD patterns for both the P-PB and the 25@FLP-PB samples are nearly identical, showing sharp diffraction peaks corresponding to the expected crystalline phase of the hexacyanoferrate without any secondary phases,[39] which indicates that the low-temperature MLD process did not damage the crystallinity of the cathode (Fig. S2, SI). This structural preservation is a critical advantage of the MLD technique.[40]

Direct visualization of the nanoscale coating was achieved through transmission electron microscopy (TEM). As seen in Fig. 1c, the 25@FLP-PB particle is uniformly covered by a smooth, conformal artificial CEI layer with a thickness of approximately 8 nm. This result highlights the precision of the MLD technique in creating homogeneous surface layers, which is crucial for uniform ion flux and stable long-term cycling.[41] In contrast, the pristine PB cathode shows a bare, unmodified surface (Fig. S3, SI). Energy-dispersive X-ray spectroscopy (EDS) mapping further corroborates these findings (Fig. S4, SI). While the native elements (Fe, C, N) are uniformly distributed throughout the core of both pristine and coated hexacyanoferrate particles, the 25@FLP-PB sample, owing to the absence of Fe in the coating layer, shows a distinct interface that confirms the presence of the surface layer.

The surface chemistry of the coating was also elucidated using XPS. The high-resolution N 1s spectrum of the 25@FLP-PB sample (Fig. 1d) reveals two distinct peaks. The peak at 398 eV, present in both samples, is assigned to the C≡N cyanide bond of the PB framework. Crucially, the peak at 399.5 eV, which is unique to the coated sample, corresponds to the NH–C(═O)– bond, providing definitive evidence of the urea linkage in the FLP film.[34] Analysis of the C 1s and O 1s core-level spectra (Fig. S5, SI) reveals a significant attenuation in signal intensity for the coated samples compared to the uncoated substrate. This decrease is directly attributed to the encapsulation of the PB particles by the artificial coating. As a surface-sensitive technique, the XPS results show that the artificial FLP coating effectively masks the underlying PB particle substrate, reducing its detectable signal.

Finally, to investigate the impact of the coating on the active material, X-ray absorption spectroscopy (XAS) was utilized to probe both the electronic and local atomic structure. The Fe K-edge X-ray Absorption Near-Edge Structure (XANES) spectra for the pristine and FLP-coated hexacyanoferrate samples are presented in Fig. 1e. The spectra are virtually superimposable, a finding with a twofold implication. First, the identical energy position of the absorption edge confirms that the average oxidation state of the Fe centers is unaffected by the deposition. Second, the perfect congruence in the spectral shape demonstrates that the local coordination environment and geometry around the iron atoms are also preserved after coating. This comprehensive analysis confirms the FLP coating behaves as an ideal, conformal physical-barrier layer, leaving both the fundamental electronic and structural integrity of the active material pristine.

To evaluate the impact of the artificial CEI on the Na storage properties of the hexacyanoferrate cathode, a series of electrochemical tests was performed on cells assembled with both P-PB and FLP-coated cathodes. Long-term cycling stability, a critical metric for practical applications, was evaluated by testing cathodes coated with different MLD cycles (10, 25, and 50) at both high (5C) and low (1C) current densities (Fig. 2a and b). At the high rate of 5C, the 25@FLP-PB coating significantly improves cycling stability compared to the uncoated PB, as shown in Fig. 2a. Although the pristine sample exhibits a higher initial specific capacity (~112 mAh g^{-1}), its capacity decreases rapidly with cycling, dropping below that of 25@FLP-PB after approximately 500 cycles. The effect of coating thickness was also systematically evaluated, revealing that the 25-cycle FLP layer reflects an optimal balance between interfacial passivation/mechanical buffering and interfacial transport/contact penalties. Interphase thickness is widely recognized as a critical parameter because it directly governs interfacial resistance and robustness. A conformal artificial interphase is essential to suppress electrolyte decomposition and stabilize CEI evolution, but it can also increase initial interfacial impedance and polarization when the layer becomes excessively thick or less ion-permeable.[2,42,43] The thinner 10@FLP-PB coating offered better performance than the pristine sample, but its stability was not as robust as the 25-cycle layer. Increasing the coating thickness to 50 cycles (50@FLP-PB) did not improve stability and reduced the capacity to 90 mAh g^{-1}, likely due to increased ionic diffusion resistance, which highlights the importance of precise, nanoscale control over the coating thickness. Beyond diffusion resistance alone, thicker polymer coatings can lengthen the effective Na^+ transport path across the interphase (higher interfacial resistance), reduce electrolyte wetting/active surface accessibility, and deteriorate electronic/ionic transport pathways in the composite cathode electrode, collectively lowering rate capability and accessible capacity.[44] The 25@FLP-PB sample, exhibiting the most stable discharge capacity, was tested for an extended duration and delivered a discharge capacity of 64 mAh g^{-1} at 5C with an exceptionally high Columbic efficiency (~99.8%) after 3000 cycles. This level of durability is comparable to the best-performing coated PBA systems reported.[45] To benchmark the long-term cycling stability achieved here against recent PBA interphase/coating strategies, a summary comparison is provided in Table S1 (SI) to contextualize the advancement of our work relative to prior reports.[6,21,28,30,45–47] Additional evaluations at a lower current density of 1C corroborate this enhanced stability; while the P-PB cathode initially delivers a comparable capacity, it undergoes pronounced and accelerated decay, falling below the 25@FLP-PB sample after approximately 250 cycles (Fig. 2b). This enhanced durability and stability in cycling performance of the coated sample arises from the stable artificial CEI, which protects the active material from degradation, a primary goal of surface engineering strategies.[40] Rate capability was further evaluated by stepwise cycling at 0.1C–10C (Fig. S6, SI). During the initial low-rate steps (0.1C–2C), pristine PB and 25@FLP-PB deliver comparable capacities. Upon repeated high-rate steps (5C and 10C), 25@FLP-PB retains higher and more stable capacities and improved recovery relative to pristine PB. This behavior is consistent with the FLP coating stabilizing interphase evolution and suppressing polarization growth during fast cycling.

The evolution of the voltage profiles over extended cycling further illustrates the stabilizing effect of the FLP coating. The voltage profiles for P-PB and 25@FLP-PB at 10st, 100th, 500th, 1000th, 1500th, 2000th, and 2500th cycles are demonstrated in Fig. 2c. The profiles for the P-PB cathode show continuous and accelerating capacity fade, particularly after 500 cycles. This degradation is dramatically mitigated in the 25@FLP-PB sample, which maintains stable voltage plateaus, indicating the preservation of the electrode's structural and electrochemical integrity. To quantitatively pinpoint the source of this stability, the discharge profiles at 5C for 100th, 500th, and 1000th cycles were deconvoluted into contributions from the two distinct redox plateaus (Fig. S7, SI). For the P-PB sample, the capacities from both the high-spin (~2.8 V) and low-spin

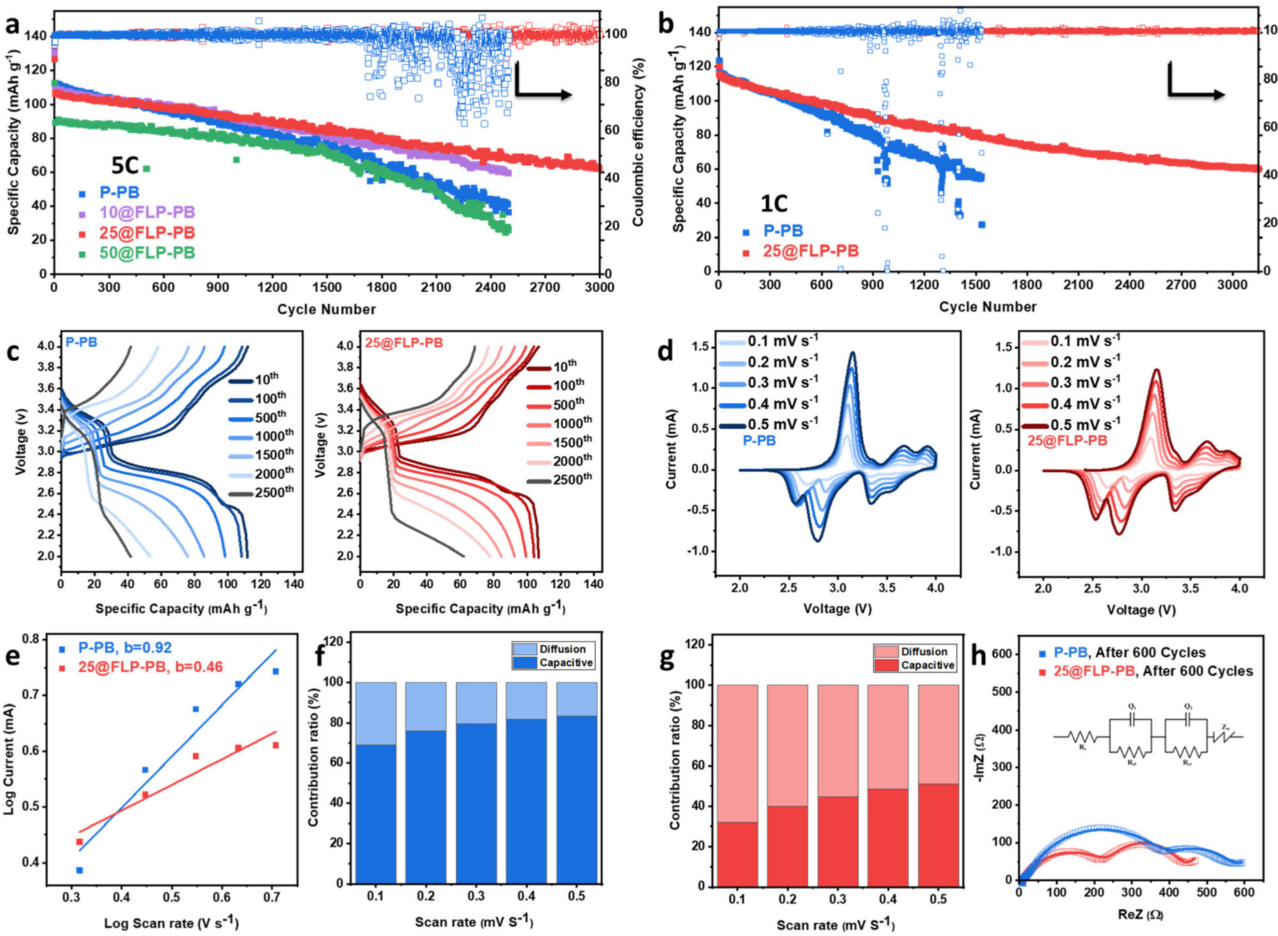

Fig. 2 (a) Long-term cycling performance at a high rate of 5C, comparing different FLP coating thicknesses. (b) Long-term cycling performance at a low rate of 1C. (c) Evolution of voltage profiles for the P-PB and 25@FLP-PB samples at various cycle numbers. (d) Cyclic voltammetry curves for P-PB and 25@FLP-PB electrodes. (e) Corresponding log(i) *vs.* log(ν) plots for the determination of the b-value. Contribution ratios of capacitive and diffusion-controlled processes at 0.5 mV s^{-1} for (f) P-PB, and (g) 25@FLP-PB. (h) Nyquist plots of P-PB and 25@FLP-PB electrodes after 600 cycles.

(~3.1 V) Fe redox sites decay significantly over 1000 cycles. At the 100th cycle, these plateaus deliver 30.71 and 108.47 mAh g^{-1}, respectively, which decline to 23.62 and 85.87 mAh g^{-1} by the 1000th cycle. In stark contrast, the low-spin plateau of the 25@FLP-PB sample remains remarkably stable, delivering a constant capacity of 21.19 mAh g^{-1} across 1000 cycles. While the high-spin plateau still exhibits some capacity fade, likely due to the sluggish extraction of coordinated water from high-spin Fe (Fe–N) sites, the decay rate is lower than in the pristine cathode, and the second plateau persists longer. Crucially, this decay is governed not only by intrinsic crystal defects or the zeolitic/coordinated water content of PBAs, but also by irreversible crystal/structural changes that accumulate during cycling.[48] The flexible polymer coating does not fully stabilize the second plateau; however, by accommodating lattice strain and moderating volume fluctuations, it partially inhibits water loss, limits framework degradation, suppresses parasitic reactions, and thereby slows the fading of discharge capacity.

To elucidate the kinetic origins of this enhanced performance, the mechanisms of Na ion transport were investigated. The fundamental electrochemical behavior was first assessed by cyclic voltammetry (CV) at various scan rates (Fig. 2d). Both electrodes exhibit the characteristic redox peaks for Fe-based hexacyanoferrates: the peaks around 2.8 V correspond to the high-spin Fe^{2+}/Fe^{3+} (N-coordinated) redox couple, while the peaks at approximately 3.3 V are attributed to the low-spin Fe^{2+}/Fe^{3+} (C-coordinated) couple.[48] Additional cathodic peaks around 2.5 V for both samples might be caused by Na^{+} extracted/inserted from some other sites in the structure.[49] The relationship between peak current (i) and scan rate (ν) was analyzed using the power-law equation, $i = a\nu^{b}$, to distinguish between diffusion-controlled (b = 0.5) and surface capacitive-controlled (b = 1.0) processes.[50] As shown in Fig. 2e, the P-PB electrode exhibits an apparent b-value of 0.92, indicating that the measured current within the selected scan-rate window is dominated by a large surface-accessible contribution. In defect- and water-rich PB, electrolyte-accessible Fe sites and structural water can promote fast near surface redox responses, and the extracted surface-controlled current can also include contributions from interfacial processes (*e.g.*, concurrent electrolyte/CEI side reactions), which may bias the fitted *b*-value toward unity. In contrast, the 25@FLP-PB electrode shows a lower apparent *b*-value (0.46), indicating that the electrochemical kinetics is increasingly governed by diffusion-associated Na^+ insertion/extraction rather than fast surface-dominated pathways. We note that the *b*-value is obtained from the empirical power-law relationship ($i = a\nu^b$) where $b \approx 1$ and $b \approx 0.5$ correspond to surface-controlled and diffusion-controlled limits, respectively, and slight deviations from 0.5 can occur in real electrodes due to mixed kinetics, peak overlap, and polarization effects. Importantly, the decrease in *b* does not imply that the FLP coating blocks Na^+ transport; rather, it is consistent with surface passivation that suppresses unstable surface contributions and promotes more reversible bulk insertion. This interpretation is supported by Dunn's quantitative separation (Fig. 2f and g) as well as by the comparable GITT-derived Na^+ diffusion coefficients and the reduced interfacial/charge-transfer resistances (EIS), which together indicate that Na^+ transport remains accessible while the interface becomes more stable. The Na^+ storage mechanisms during the charge–discharge process are also schematically illustrated in Fig. S8 (SI) for both samples. At a scan rate of 0.5 mV s^{-1}, the 25@FLP-PB cathode clearly demonstrates a hybrid capacitive–diffusion-controlled behavior, consistent with enhanced kinetic stability and sustained electrochemical performance.

Galvanostatic intermittent titration technique (GITT) was also employed to obtain a quantitative measure of the Na^+ diffusion coefficient (D_{Na^+}), as shown in Fig. S9, SI. Although P-PB and 25@FLP-PB exhibit similar calculated D_{Na^+} values, likely reflecting their inherently open frameworks, the 25@FLP-PB electrode exhibits more stable diffusion behavior during cycling, confirming that the FLP coating facilitates consistent and sustained Na^+ transport kinetics. The structural and interfacial evolution of the cathodes before and after prolonged cycling for P-PB and 25@FLP-PB was further investigated using electrochemical impedance spectroscopy (EIS), as shown in Fig. 2h and Fig. S10, SI, respectively. Notably, the fresh 25@FLP-PB cell exhibits a higher initial impedance than P-PB (Fig. S10, SI), consistent with an additional interfacial film introduced by the polymer coating. After 600 cycles, equivalent-circuit fitting reveals two semicircles are observed in the high and medium frequency regions, respectively (Fig. 2h). The high-frequency intercept corresponds to the internal resistance (R_s), which reflects the combined contributions from the electrolyte, separator, and electrode components. The high-frequency semicircles, where the R_{ct} and R_f denote the charge transfer resistance and interfacial resistance, respectively.[51,52] Notably, the charge transfer resistance, R_{ct}, and interfacial resistance, R_f, of the pristine electrode are significantly higher than those of the 25@FLP-PB electrode. This indicates that without protection, a thick, resistive, and unstable natural CEI forms on the cathode, impeding both charge transfer and Na^+ migration.[45] The FLP coating successfully prevents this detrimental evolution, maintaining a low-impedance interface and enabling the superior long-term performance observed. To provide quantitative evidence for interfacial Na^+ transport, we tracked the interphase resistance (R_f) at multiple states of charge during the 1st, 2nd, 5th, and 15th cycles (Fig. S11–S14, SI). Both electrodes exhibit a pronounced R_f spike at the early charging stage (2.9 V) in the first cycle, followed by a rapid decrease with cycling, consistent with initial wetting/activation and interphase formation. Importantly, the FLP-coated electrode does not show a persistent R_f penalty across subsequent state of charge (SOC) steps; instead, R_f converges is comparable to that of the pristine electrode by cycles 2–15 (and in several states similar or slightly lower). This behavior indicates that the protective FLP layer does not impose a sustained ion-transport bottleneck; rather, it promotes a more stable interphase evolution while maintaining interfacial Na^+ transport during early cycling.

To further elucidate how the FLP coating influences the interphase region and preserves particle integrity, thereby explaining the enhanced electrochemical performance, a suite of post-cycling characterizations was employed to analyze the evolution of the interfacial structure and composition after 1000 cycles. The integrity of individual particles and the nature of the CEI were first characterized by the TEM. As shown in Fig. 3a, the P-PB particles suffer from the formation of a thick, rough, and inhomogeneous CEI composed of electrolyte decomposition products. This layer fails to completely cover the particle surface, leaving exposed regions that are vulnerable to persistent side reactions with the electrolyte, a common cause of capacity fade in PBA cathodes.[41] In stark contrast, the 25@FLP-PB sample maintains a smooth, well-defined surface, indicating that the artificial coating successfully preserves the interfacial integrity during prolonged cycling (Fig. 3b).

The TEM-EDS mapping provides direct evidence of the chemical evolution at the interface of uncoated and coated cathodes during electrochemical cycling (Fig. 3, Fig. S15 and S16, SI). For both samples, the homogeneous distribution of the framework elements (Na, Fe, C, and N) confirms that the bulk PBA lattice remains largely intact. However, significant differences are observed in the composition of the interface layer. The uncoated sample exhibits blurred interfacial contrast and a patchy, heterogeneous distribution of CEI components (C, F, Cl, O), indicative of uncontrolled electrolyte decomposition, as shown in Fig. 3a and Fig. S15 (SI). Conversely, the coated sample shows a conformal and continuous CEI, with a uniform distribution of these elements (Fig. 3b and Fig. S16, SI). The uniform F, Cl, and C signals indicate the consistent formation of inorganic species (*e.g.*, Na_2CO_3, NaCl, NaF) and organic components, enhancing interfacial chemical stability.[53] Overall, these results show that while the PB framework remains intact, the FLP coating effectively regulates interfacial reactions, forming a uniform CEI that suppresses active material dissolution and promotes stable Na^+ transport.

Moving from the nanoscale interface to the microscale particle structure, SEM was used to examine the mechanical stability of the electrodes after extended cycling (Fig. 3c and d). The images reveal significant differences in structural integrity. After 1000 cycles, severe cracking is evident throughout the

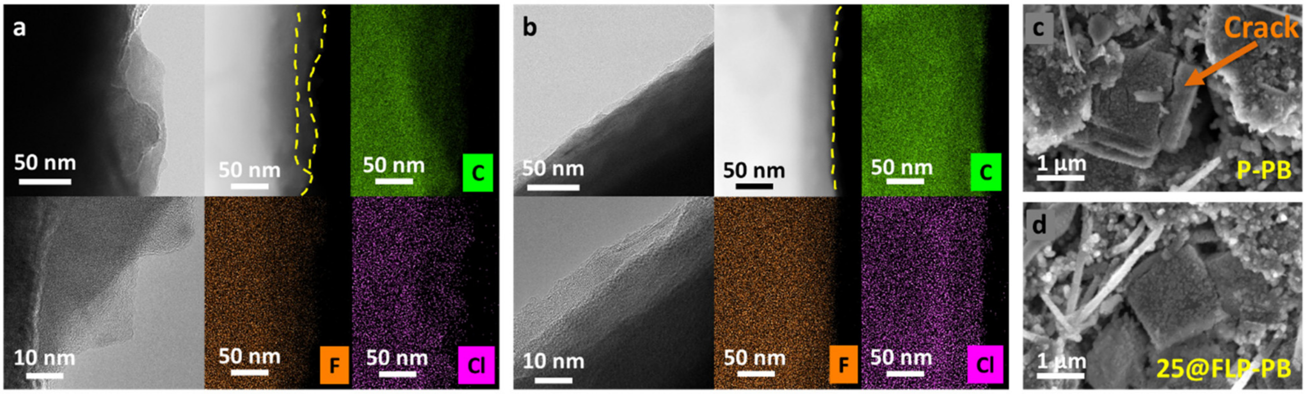

Fig. 3 High-resolution TEM images and corresponding EDS elemental mappings of the CEI formed on (a) uncoated (P-PB) and (b) coated (25@FLP-PB) cathodes. Post-cycling SEM analysis after 1000 cycles of (c) the P-PB cathode, showing severe particle cracking and degradation, and (d) the 25@FLP-PB cathode, showing well-preserved particle morphology and integrity.

P-PB surface morphology (Fig. 3c). This mechanical failure is a well-documented degradation mechanism in PBA cathodes, arising from the accumulated internal stress of repeated volume changes during sodiation and desodiation.[54] These cracks expose internal pristine active material to the electrolyte, leading to continuous CEI formation, increased impedance, and the accelerated capacity fading observed in the electrochemical data.[55] Remarkably, the 25@FLP-PB particles maintain their structural integrity with significantly fewer microcracks after the same number of cycles (Fig. 3d). For the uncoated PB sample, cracks appear even at relatively low cycle numbers (600 cycles), and with prolonged cycling (1000 and 1500 cycles), the particles progressively lose their well-defined cubic morphology, leading to severe structural degradation and collapse, as shown in Fig. S17, SI. In contrast, the coated PB sample maintains its particle integrity and shape even after extended cycling, with minimal visible cracking or surface deterioration (Fig. S18, SI). Generally, the mechanical damage mainly originates from the accumulated inner strain/stress of particles induced by the repeated volume expansions/contractions during (de)sodiation. Thanks to the desired mechanical stability, the FLP coating layer could play a buffering role on the deformation force of the PB structure to maintain the structural integrity, which is confirmed by the combined analysis of SEM and XRD results.[54]

To elucidate the mechanism underlying the enhanced cycling stability, the structural and interfacial evolution of the P-PB and 25@FLP-PB electrodes after cycling was investigated using characterization techniques, as shown in Fig. 4. The structural changes in both electrodes after 300th Na^+ insertion/extraction processes were tracked at various charge/discharge states, focusing on the key (200), (220), and (400) reflection planes, the *ex situ* XRD patterns (Fig. 4a and Fig. S19–S21, SI). An enlarged view of the (200) reflection plane highlights the significant difference in structural reversibility between the P-PB and 25@FLP-PB electrodes, as illustrated in Fig. 4a. For both electrodes, the (200) peak shifts to higher diffraction angles upon charging to 4.0 V (≈17.03°), indicating lattice contraction (decreased *d*-spacing) during Na^+ extraction; upon discharge, the peak shifts back toward lower angles, consistent with reversible lattice expansion during Na^+ reinsertion. Notably, after full discharge, the reflections of the 25@FLP-PB electrode recover closely to their initial positions with limited peak broadening, evidencing high phase/lattice reversibility and preserved crystallinity after prolonged cycling. In contrast, the P-PB electrode exhibits more pronounced peak broadening and incomplete recovery of peak position after discharge, suggesting accumulated irreversible structural distortion and/or incomplete Na^+ reinsertion (loss of active Na inventory) after extended cycling. This repeated mechanical strain leads to the accumulation of internal stress, causing particle cracking, loss of crystallinity, and eventual structural collapse, which is a primary reason for its capacity decay.[39,56] These results indicate that the FLP coating does not eliminate the intrinsic, reversible lattice breathing associated with (de)sodiation; rather, it suppresses irreversible crystallographic degradation and preserves structural coherence, thereby mitigating performance decay. The XRD analysis of the first cycle further confirms this behavior, showing that the 25@FLP-PB cathode maintains more stable peaks and structural integrity from the outset compared to the pristine hexacyanoferrate sample (Fig. S20 and S21, SI).

To investigate the dynamic structural evolution at a more localized level, *ex situ* Raman spectroscopy was employed to monitor the chemical environment of the cyanide $(C{\equiv}N)^-$ group after 1 and 300 cycles (Fig. 4b and S22, SI). This technique is particularly sensitive to the vibrational modes of the cyanide ligands and can provide insights into local structure and stress that complement the bulk information from XRD.[57] Both pristine and coated PB cathodes at the beginning of the charging stage exhibit two strong $\nu(C{\equiv}N)$ vibrational modes, near 2093 and 2131 cm^{-1}, corresponding to symmetric (ν_s) and asymmetric (ν_{as}) modes in the $Fe^{II}–C{\equiv}N–Fe^{III}$ configuration.[58,59] Further, the initial presence of the Fe^{III}-containing species in both samples before cycling is attributed to the inevitable partial oxidation of the material during synthesis. *Ex situ* Raman spectroscopy of P-PB shows clear shifts

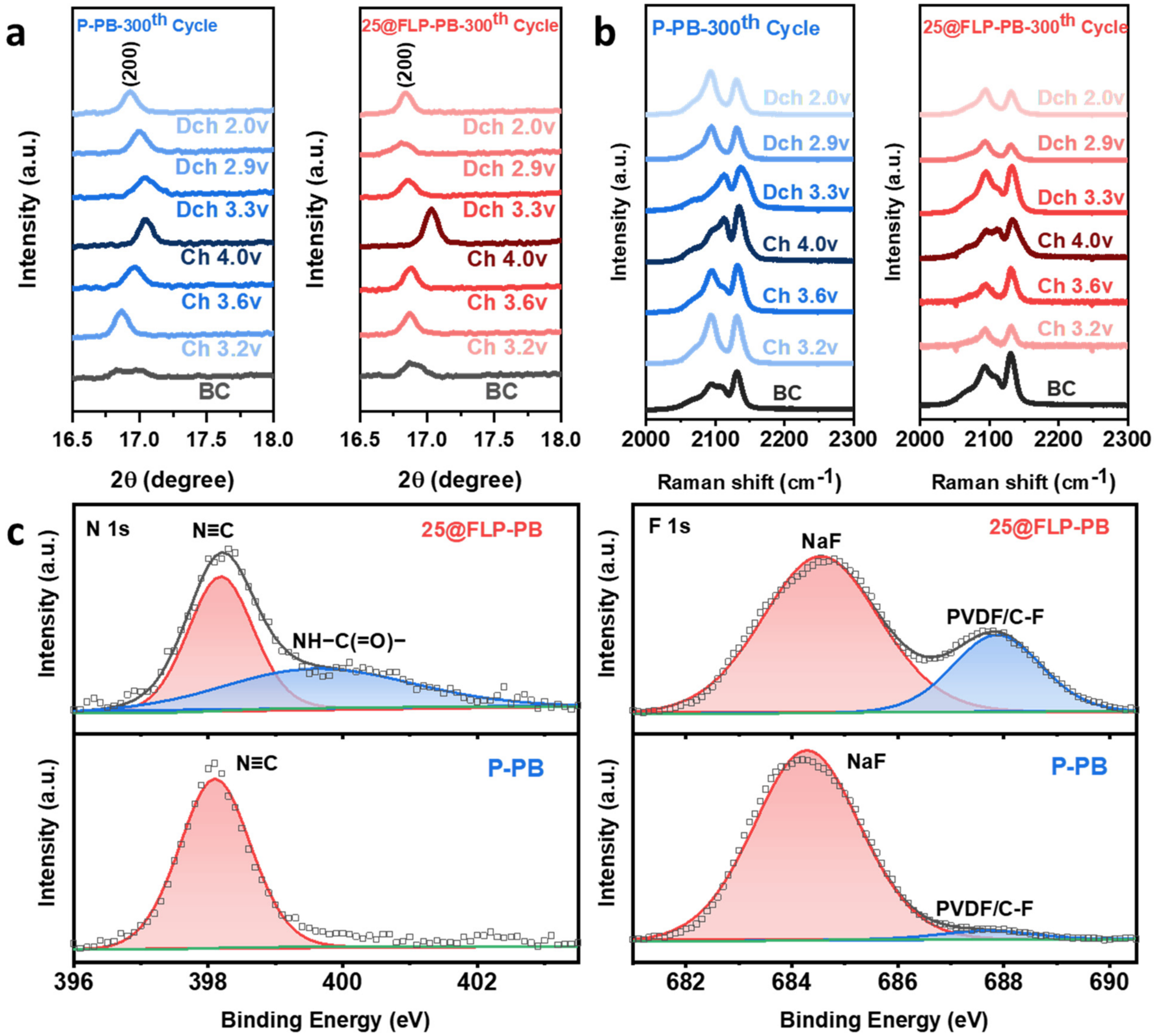

Fig. 4 Post-cycling analysis of P-PB and 25@FLP-PB electrodes. (a) *Ex situ* XRD patterns after 300 cycles. (b) *Ex situ* Raman spectra after 300 cycles. (c) Post-cycling XPS N 1s and F 1s spectra after 1000 cycles.

of the characteristic Raman ν(C$\equiv$N) modes. After 300 cycles, the vibrational modes associated with the Fe^{II}–C$\equiv$N–Fe^{III} undergo a blue shift during charging (Na^+ extraction), consistent with oxidation at high spin Fe–N sites and phonon stiffening under compressive lattice strain; conversely, discharging (Na^+ insertion) produces a red shift associated with tensile strain (Fig. 4b).[57,58,60] In stark contrast, the FLP-coated electrode (25@FLP-PB) exhibits a smaller shift window and improved reversibility of the ν(C$\equiv$N) modes, indicating that the coating effectively mitigates lattice breathing and the associated mechanical strain. During the first cycle, the uncoated PB cathode displays the same blue/red-shift trend but within a smaller shift window (Fig. S22, SI), whereas the coated PB shows less peak drift and narrower broadening, with more reversible peak-position changes.

Furthermore, to gain a deep understanding of the interface chemistry that drives the enhanced stability, XPS was applied to analyze the CEI on the 25@FLP-PB and P-PB electrodes after 1000 cycles (Fig. 4c and S23, SI). A critical finding is observed in the N 1s spectrum (Fig. 4c), where the peak around 400 eV, assigned to amide/amine nitrogen in the urea linkage, is clearly present on the 25@FLP-PB electrode but absent on the pristine sample. This result unequivocally confirms that the robust FLP coating still remains on the cathode surface, serving as a foundational component of the artificial CEI even after extensive cycling.[32] The slight decrease in peak intensity compared to the uncycled sample is likely due to reactions with active species in the electrolyte or interstitial water in the PB structure, but the persistence of the urea signature is a testament to the coating's chemical stability. In the F 1s region, both electrodes exhibit F-containing CEI components, including a low-binding-energy contribution consistent with an inorganic fluoride (NaF-like) species, which is commonly associated with a more stable interphase in Na-ion systems.[45] The 25@FLP-PB electrode shows a more pronounced

F-containing signal together with stronger organic components in the C 1s and O 1s spectra in the CEI composition (Fig. S23, SI) compared with the pristine electrode. The FLP coating has been involved in the formation of the CEI. Because of the PVDF binder in the electrodes, deconvoluting the precise origin of individual C–F and C–O features is inherently non-trivial; therefore, we interpret these signals conservatively in terms of CEI composition and interphase robustness rather than assigning them to a specific formation pathway. Collectively, the persistence of the urea-linkage signature together with the NaF-rich interphase indicates that the FLP functions primarily as a conformal, mechanically compliant scaffold that passivates reactive sites and stabilizes the interface. The polar urea groups may also plausibly regulate CEI evolution *via* dipole/hydrogen-bonding interactions with interfacial species.

The combination of these findings suggests that the FLP coating facilitates the formation of a superior hybrid organic-inorganic CEI. While the pristine surface leads to uncontrolled electrolyte decomposition, the FLP coating directs the formation of a more stable interface rich in both NaF and flexible organic species.[26] These organic components are critical as they impart mechanical compliance to the CEI, which is vital for accommodating the volumetric expansion and contraction the cathode material undergoes during repeated cycling. The creation of such a robust and flexible artificial interface is a key strategy for enabling long-life, high-energy batteries.[56,61] Although we did not directly quantify the mechanical properties (*e.g.*, modulus/adhesion) of the FLP film in this work, the polyurea-based MLD coatings have been approved as mechanically robust yet compliant interphases owing to their flexible polymer chains and extensive hydrogen-bonding networks.[33] Compared with rigid inorganic coatings (*e.g.*, metal oxides), polymeric/MLD interphases are generally softer and more flexible, which can better accommodate repeated volume fluctuations without cracking or delamination; accordingly, MLD polyurea coatings have a low stifness and high flexibility compared to the inorganic metal oxides, which can accommodate the massive volume changes of electrodes without immediate fracture.[62] In this context, the reduced microcracking and improved structural reversibility observed here are consistent with suppressed chemo-mechanical degradation enabled by a compliant, conformal FLP interphase.

While Na-metal half-cells isolate cathode-specific behavior, practical Na-ion full cells are constrained by a finite Na-inventory. Because the cathode is the primary Na^+ source, continuous consumption during CEI formation directly reduces capacity and cycle life. Full-cell compatibility, particularly when paired with hard carbon, also requires mitigating gas evolution and impedance growth linked to residual water and side reactions in PBAs.[49,63] Furthermore, moving toward high energy density requires increased areal loading and electrode density, which typically exacerbates interfacial instability and resistance growth over time.[41] The conformal FLP artificial CEI addresses these practical hurdles by stabilizing the interface and suppressing continuous electrolyte decomposition. By conserving the active Na inventory and limiting impedance rise, this interphase-stabilization approach provides a clear pathway for integrating PBA cathodes into long-lived, high-loading full cells.

Conclusion

In summary, we demonstrate a nanoscale FLP artificial CEI that addresses chemo-mechanical degradation in Fe-based PBA cathodes. The conformal, nanometric interphase serves as a robust physicochemical barrier: by buffering (de)sodiation-induced volume change and passivating the surface against electrolyte attack, it preserves bulk lattice integrity and surface chemistry, mitigating active-material dissolution and conserving the Na^+ inventory. As a result, the coated electrodes demonstrate much more stable performances over 3000 cycles at 5C. Volumetric-change and surface-morphology analyses show faceted particle integrity with suppressed microcrack initiation and intergranular voiding, evidencing effective strain accommodation and improved electrode cohesion relative to uncoated controls. Post-cycling structural and interfacial probes corroborate this mechanism, revealing reduced lattice-breathing hysteresis, as evidenced by smaller XRD peak shifts and attenuated Raman-band drift, more uniform and chemically robust CEI layer with fewer electrolyte-decomposition signatures, and stabilized charge-transfer/interfacial resistances. Collectively, these observations indicate more homogeneous Na^+ transport and a durable interphase that decouples crystallographic breathing from parasitic chemistry. Ultimately, this work moves beyond a single coating recipe to establish generalizable design principles for PBA interphases, prioritizing conformality, mechanical compliance, and controlled thickness, and offers a scalable, chemistry-agnostic route to durable, high-performance, low-cost Na-based energy storage.

Author contributions

P. P. and Y. Z. conceived and designed the experiments. P. P. prepared samples and carried out the main experiments. E. J. and Y. W. helped with the ALD deposition. Z. D., Y. G., Y. Y., S. A. C. and L. Y. C. helped with the synchrotron measurements and data analysis. M. Y., R. A. F. H., X. P. were involved in data analysis. P. P. wrote and Y. Z. revised the paper. All the authors commented on the manuscript.

Conflicts of interest

There are no conflicts to declare.

Data availability

The data supporting this article have been included as part of the supplementary information (SI). Supplementary information is available. See DOI: https://doi.org/10.1039/d6eb00031b.

Acknowledgements

This research was supported by the Natural Science and Engineering Research Council of Canada (NSERC), the Canada Foundation for Innovation (CFI), the Ontario Research Fund (ORF), Mitacs and the University of Western Ontario (UWO). Synchrotron measurements were conducted at the TLS beamline 07A at the Taiwan Light Source (TLS).

References

1 M. Yang, *et al.*, The review of sodium and potassium-ion battery advances in density functional theory: Progresses, challenges and prospects, *Mater. Sci. Eng., R*, 2026, **167**, 101097.

2 Y. Dou, *et al.*, High-abundance and low-cost anodes for sodium-ion batteries, *Carbon Neutralization*, 2024, **3**(6), 954–995.

3 A. Namazbay, *et al.*, Towards high-performance sodium-ion batteries: A comprehensive review on $Na_xNi_yFe_zMn_{1-(y+z)}O_2$ cathode materials, *Energy Storage Mater.*, 2025, **77**, 104212.

4 C. Peng, *et al.*, Recent progress of promising cathode candidates for sodium–ion batteries: current issues, strategy, challenge, and prospects, *Small Struct.*, 2023, **4**(10), 2300150.

5 S. Xu, *et al.*, Promising cathode materials for sodium-ion batteries from lab to application, *ACS Cent. Sci.*, 2023, **9**, 2012–2035.

6 Y. Xiao, *et al.*, Prussian blue analogues for sodium–ion battery cathodes: a review of mechanistic insights, current challenges, and future pathways, *Small*, 2024, **20**(35), 2401957.

7 X. Lin, *et al.*, Hydrophobic Lattice Engineering of Prussian Blue Analogs with Accelerated Redox Kinetics for High-Areal-Capacity Sodium-Ion Battery Electrodes, *ACS Nano*, 2025, **19**(34), 31023–31037.

8 Y. Liu, *et al.*, Ultrastable Fe-based prussian blue analogs cathode for sodium-ion battery, *J. Electrochem. Soc.*, 2024, **171**(11), 110518.

9 B. Zhou, *et al.*, Bulk and Interface Engineering of Prussian Blue Analogues Cathodes for High-Performance Sodium-Ion Batteries, *Chem. Sci.*, 2025, **16**(30), 13594–13628.

10 T.-U. Wi, *et al.*, Cathode electrolyte interphase engineering for Prussian blue analogues in lithium-ion batteries, *Nano Lett.*, 2024, **24**(25), 7783–7791.

11 J. R. Fitzpatrick, *et al.*, An in–depth Study of the Solid Electrolyte Interphase Compositional Evolution in Sodium–Ion Batteries: Unravelling the Effects of a Na Metal Counter Electrode on the SEI, *Adv. Sci.*, 2025, e04717.

12 Z. Zhang, *et al.*, Research progress on electrolyte additives for sodium ion batteries, *Sustain. Polym. Energy*, 2024, **2**(1), 10003.

13 I. Moeez, *et al.*, Artificial cathode electrolyte interphase by functional additives toward long-life sodium-ion batteries, *Chem. Eng. J.*, 2021, **425**, 130547.

14 S. Huang, *et al.*, Solvation Structure and Interface Engineering Synergy in Low-Temperature Sodium-Ion Batteries: Advances and Prospects, *Nanomaterials*, 2025, **15**(11), 820.

15 W. Li, *et al.*, Insights on the degradation mechanism of 7 Ah sodium ion batteries at different aging modes, *J. Power Sources*, 2025, **639**, 236635.

16 H. Khezraqa, M. Golshan and M. Salami-Kalajahi, Solid/electrolyte and cathode/electrolyte interphases in rechargeable ion batteries: Challenges and perspectives, *Appl. Energy*, 2025, **384**, 125509.

17 Y. He, Z. Chen and Y. Zhang, Strategies for improving cathode electrolyte interphase in high-performance dual-ion batteries, *Iscience*, 2024, **27**(8), 110491.

18 L. Ge, *et al.*, Elaborating the crystal water of Prussian blue for outstanding performance of sodium ion batteries, *ACS Nano*, 2024, **18**(4), 3542–3552.

19 J. Liu, *et al.*, Vacancies–regulated Prussian Blue Analogues through Precipitation Conversion for Cathodes in Sodium–ion Batteries with Energy Densities over 500 Wh/kg, *Angew. Chem.*, 2024, **136**(39), e202400214.

20 L. Xu, *et al.*, Suppressing vacancies and crystal water of sodium manganese iron-based Prussian blue analogue by potassium doping for advanced sodium-ion batteries, *Chem. Eng. Sci.*, 2025, **302**, 120848.

21 Z.-Y. Chen, *et al.*, Synergistic modification of Fe-based Prussian blue cathode material based on structural regulation and surface engineering, *ACS Appl. Mater. Interfaces*, 2022, **14**(38), 43308–43318.

22 E. Li, *et al.*, Double additive electrolyte solvation engineering to achieve long cycle and high capacity sodium-ion battery, *Chem. Eng. J.*, 2024, **489**, 151525.

23 J. Jang, *et al.*, Anion Effects on Crystal Water Reactivity and Cathode–Electrolyte Interphase of Prussian Blue in Sodium–Ion Batteries, *Small Methods*, 2025, 2500827.

24 M. Wu, *et al.*, Anion-Induced Uniform and Robust Cathode–Electrolyte Interphase for Layered Metal Oxide Cathodes of Sodium Ion Batteries, *ACS Appl. Mater. Interfaces*, 2024, **16**(12), 15586–15595.

25 J. Liu, *et al.*, In situ construction of uniform and robust cathode-electrolyte interface toward high-stable P2-Type sodium layered oxide cathodes, *J. Power Sources*, 2023, **580**, 233435.

26 Y. Zhang, *et al.*, Air-stable prussian white cathode materials for sodium-ion batteries enabled by ZnO surface modification, *ACS Appl. Mater. Interfaces*, 2024, **16**(13), 15649–15656.

27 Q. Liu, *et al.*, A polyaniline surface-modified Prussian blue analogue cathode for flexible aqueous Zn-ion batteries, *Chem. Commun.*, 2022, **58**(59), 8226–8229.

28 Q. Zhang, *et al.*, Surface engineering induced core-shell Prussian blue@ polyaniline nanocubes as a high-rate and long-life sodium-ion battery cathode, *J. Power Sources*, 2018, **395**, 305–313.

29 Q. Xue, *et al.*, Polypyrrole-modified Prussian blue cathode material for potassium ion batteries *via* in situ polymeriz-

ation coating, *ACS Appl. Mater. Interfaces*, 2019, **11**(25), 22339–22345.

30 Y. Tang, *et al.*, Polypyrrole-promoted superior cyclability and rate capability of Na x Fe [Fe (CN) 6] cathodes for sodium-ion batteries, *J. Mater. Chem. A*, 2016, **4**(16), 6036–6041.

31 S. N. Uddin and Y. Nagao, Multilayer growth of porphyrin-based polyurea thin film using solution-based molecular layer deposition technique, *Langmuir*, 2017, **33**(44), 12777–12784.

32 T. Mu, *et al.*, Long-life silicon anodes by conformal molecular-deposited polyurea interface for lithium ion batteries, *Nano Energy*, 2022, **103**, 107829.

33 Y. Sun, *et al.*, A novel organic "Polyurea" thin film for ultralong–life lithium–metal anodes *via* molecular–layer deposition, *Adv. Mater.*, 2019, **31**(4), 1806541.

34 Y. Sun, *et al.*, A breathable inorganic–organic interface for fabricating a crack-free nickel-rich cathode with long-term stability, *Energy Environ. Sci.*, 2024, **17**(14), 5124–5136.

35 L. Habib, *et al.*, Interface and structural modulation stabilization strategies for layered transition metal oxide cathodes in sodium-ion batteries, *Energy Storage Mater.*, 2026, 104863.

36 L. Habib, *et al.*, MoS2-based anodes for sodium-ion batteries: Recent developments and key engineering approaches, *J. Energy Storage*, 2025, **139**, 118821.

37 J. Li, *et al.*, Synergistic electron highways and mechanical buffering in a dual-carbon confined MoS2 anode for superior sodium-ion storage, *Chem. Eng. J.*, 2026, 173031.

38 Y. Chen, *et al.*, Functionalization of multiwalled carbon nanotubes with uniform polyurea coatings by molecular layer deposition, *Carbon*, 2015, **82**, 470–478.

39 S. Qiao, *et al.*, Structure defects engineering in Prussian blue cathode materials for high-performance sodium-ion batteries, *J. Alloys Compd.*, 2023, **950**, 169903.

40 H. Zhang, *et al.*, Long–cycle–life cathode materials for sodium–ion batteries toward large–scale energy storage systems, *Adv. Energy Mater.*, 2023, **13**(23), 2300149.

41 J. Zhang, *et al.*, Critical review on cathode electrolyte interphase towards stabilization for sodium-ion batteries, *Nano Energy*, 2024, **128**, 109814.

42 Y. Wang, *et al.*, Insight into the Interface Design for Li Metal Anode: Organic–Rich or Inorganic–Rich, *Adv. Funct. Mater.*, 2024, **34**(46), 2406426.

43 P. Pirayesh, *et al.*, From Nanoalloy to Nano–Laminated Interfaces for Highly Stable Alkali–Metal Anodes, *Adv. Mater.*, 2023, **35**(29), 2301414.

44 Y. Huang, *et al.*, Electrolytes and electrolyte/electrode interfaces in sodium–ion batteries: from scientific research to practical application, *Adv. Mater.*, 2019, **31**(21), 1808393.

45 M. Ye, *et al.*, *In situ* construction of a NaF-rich cathode–electrolyte interface on Prussian blue toward a 3000-cycle-life sodium-ion battery, *Mater. Today Energy*, 2022, **23**, 100898.

46 C. Xu, *et al.*, Surface Engineering Stabilizes Rhombohedral Sodium Manganese Hexacyanoferrates for High–Energy Na–Ion Batteries, *Angew. Chem.*, 2023, **135**(13), e202217761.

47 X. Y. Fu, *et al.*, Achieving a superior Na storage performance of Fe–based Prussian blue cathode by coating perylene tetracarboxylic dianhydride amine, *Carbon Energy*, 2024, **6**(5), e446.

48 H. Zhang, *et al.*, Understanding capacity fading from structural degradation in Prussian blue analogues for wide-temperature sodium-ion cylindrical battery, *Nat. Commun.*, 2025, **16**(1), 2520.

49 W. Wang, *et al.*, Reversible structural evolution of sodium-rich rhombohedral Prussian blue for sodium-ion batteries, *Nat. Commun.*, 2020, **11**(1), 980.

50 M. Qin, *et al.*, Highly crystallized Prussian blue with enhanced kinetics for highly efficient sodium storage, *ACS Appl. Mater. Interfaces*, 2021, **13**(3), 3999–4007.

51 W. Li, *et al.*, Stress distortion restraint to boost the sodium ion storage performance of a novel binary hexacyanoferrate, *Adv. Energy Mater.*, 2020, **10**(4), 1903006.

52 Y. Gao, *et al.*, Structural Modulation of Cu–Mn–Fe Prussian Blue Analogs for Practical Sodium Ion Cylinder Cells, *Adv. Mater.*, 2025, 2417876.

53 X. Ji, H. Hou and G. Zou, *Sodium-Ion Batteries: Technologies and Applications*, John Wiley & Sons, 2023.

54 Y. Huang, *et al.*, Modification of Prussian blue analogues as high-performance cathodes for sodium-ion batteries, *Chem. Eng. J.*, 2024, **499**, 156410.

55 H. Bi, *et al.*, Tailoring Cathode Interfaces in Sodium–Ion Batteries: Advanced Coating Strategies and Electrochemical Interface Regulation, *Adv. Funct. Mater.*, 2025, e07781.

56 X. Liang, *et al.*, High-energy and long-life O3-type layered cathode material for sodium-ion batteries, *Nat. Commun.*, 2025, **16**(1), 3505.

57 K. Sada, *et al.*, Deciphering the local structure of Prussian blue analogue cathodes with Raman spectroscopy for sodium-ion batteries, *J. Mater. Chem. A*, 2025, **13**(28), 22903–22914.

58 K. Sada, *et al.*, Unveiling the influence of water molecules on the structural dynamics of prussian blue analogues, *Small*, 2024, **20**(50), 2406853.

59 J. Peng, *et al.*, Defect–healing induced monoclinic iron–based prussian blue analogs as high–performance cathode materials for sodium–ion batteries, *Small*, 2023, **19**(36), 2300435.

60 H. Li, *et al.*, Operando electrochemical X-ray diffraction and Raman spectroscopic studies revealing the alkali-metal ion intercalation mechanism in Prussian blue analogues, *J. Phys. Chem. Lett.*, 2022, **13**(2), 479–485.

61 A. Belous, I. Lisovskyi and V. Khomenko, Surface modification of cathode materials with functional coatings for enhanced lithium-ion battery durability, *J. Appl. Electrochem.*, 2025, 1–34.

62 Y. Sun, *et al.*, Tailoring the mechanical and electrochemical properties of an artificial interphase for high–performance metallic lithium anode, *Adv. Energy Mater.*, 2020, **10**(28), 2001139.

63 J. Peng, *et al.*, Prussian blue analogues for sodium–ion batteries: past, present, and future, *Adv. Mater.*, 2022, **34**(15), 2108384.